Exsolution of Catalytically Active Iridium Nanoparticles from Strontium Titanate

Eleonora Calì[†]*, Gwilherm Kerherve[†], Faris Naufal[†], Kalliopi Kousi[‡], Dragos Neagu[‡], Evangelos I. Papaioannou[‡], Melonie P. Thomas[§], Beth S. Guiton[§], Ian S. Metcalfe[‡], John T. S. Irvine[||], David J. Payne[†]*

[†]Department of Materials, Imperial College London, Exhibition Road, London SW7 2AZ, United Kingdom

[‡]School of Engineering, Newcastle University, Merz Court, Newcastle upon Tyne NE1 7RU, United Kingdom

[§]Department of Chemistry, University of Kentucky, 505 Rose Street, Lexington, Kentucky 40506, USA

[||]School of Chemistry, University of St Andrews, St Andrews, KY16 9ST, United Kingdom

ABSTRACT: The search for new functional materials that combine high stability and efficiency with reasonable cost and ease of synthesis is critical for their use in renewable energy applications. Specifically in catalysis, nanoparticles, with their high surface-to-volume ratio, can overcome the cost implications associated with otherwise having to use large amounts of noble metals. However, commercialized materials, i.e. catalytic nanoparticles deposited on oxide supports, often suffer from loss of activity due to coarsening and carbon deposition during operation. Exsolution has proven to be an interesting strategy to overcome such issues. Here the controlled emergence, or exsolution, of faceted iridium nanoparticles from a doped $SrTiO_3$ perovskite is reported and their growth preliminary probed by in situ electron microscopy. Upon reduction of $SrIr_{0.005}Ti_{0.995}O_3$ the generated nanoparticles show embedding into the oxide support, therefore preventing agglomeration and subsequent catalyst degradation. The advantages of this approach are the extremely low noble metal amount employed (~0.5% weight) and the catalytic activity reported during CO oxidation tests, where the performance of the exsolved $SrIr_{0.005}Ti_{0.995}O_3$ is compared to the activity of a commercial catalyst with 1% loading (1% Ir/Al_2O_3). The high activity obtained with such low-doping shows the possibility for scaling up this new catalyst, reducing the high cost associated with iridium-based materials.

INTRODUCTION

A major challenge in materials chemistry is the discovery of new functional materials that display greater resistivity to degradation and loss of efficiency. Traditionally, metal nanoparticles (NPs) dispersed on surfaces of porous crystals are of fundamental interest in fields such as catalysis, energy conversion and energy storage. [1, 2] Conventionally used "top-down" deposition techniques, however, result in nanoparticles with limited control of their size, distribution and anchorage to the surface. As a consequence, the tendency of the nanoparticles to coarsen and aggregate over time under standard operating conditions is often observed, resulting in significant performance degradation. [3] This is why the recent discovery of so-called "exsolved" nanoparticles, that is metal atoms that segregate to the surface in a controlled fashion from sites within a host perovskite lattice, have been the subject of significant scientific interest. [4–6] The perovskite oxide family, with its ABO_3 stoichiometry, is being explored extensively for possible tailored functional materials due to the structural and compositional versatility which allows A- and B-site substitution, as well as a high tolerance for defects in the crystal structure. In the last few years this "in situ" nanoparticle growth method has been developed so that NPs are grown from a doped perovskite oxide under controlled reducing conditions. The metal dopant, on either the A or the B site of the perovskite, segregates from the host structure, diffusing through the bulk before forming socketed nanoparticles on the oxide surface. [7] Among the advantages of this method, is that exsolved NPs are homogeneously distributed in size and surface density, and the socketing into the surface of the perovskite support results in enhanced thermal and hydrocarbon/coking stability, as well as strain thereby potentially enhancing activity. [5,6] Following this approach, numerous transition metals, such as Ni, [7, 8] Pd, [9] Ru, [10, 11] Pt, [12] Co, [8] Mn, [8] Fe, [8] have been doped on the B-site of stoichiometric or A-site deficient mixed perovskite oxides and subsequently exsolved under a range of reducing atmospheres or through fast electrochemical reduction. Among the transition metals, iridium is a scarce but key element being used in a variety of applications [13] including water splitting reactions, [14–17] fuel cells, [18, 19] hydrogenation reactions, [20] methane reformation [21, 22] and auto-motive exhaust catalysis. [23–26] Specifically, CO oxidation applied in air purification and pollution control in automotive exhaust uses more than 60% of the annual production of noble metals. The commonly used catalysts are Pt, Rh, and Pd deposited on oxide supports, [27, 28] which, even though highly active, suffer from sintering and poisoning. [29] Although belonging to the same group of metals, iridium has not been extensively studied in this context, however some reports have demonstrated its high activity for automotive exhaust [30] and in particular for CO oxidation. [24, 31–34] Additionally, Ir is characterized by low toxicity and environmental impact. [35] However, scarcity and high cost of the material limit

1

the use of Ir-based catalysts, requiring smart design to obtain high performance and increased stability, while limiting the amount of noble metal required. [36] A possible approach would be, therefore, to improve catalyst morphologies to expose large surface areas. [37] Nanoparticles, due to their intrinsic high surface area to volume ratio, could help overcoming the issue. Unsupported iridium nanoparticles, however, have been reported to grow and coarsen under operating conditions (for example in OER), causing loss in activity during catalysis. [38] In this work the well-studied perovskite $SrTiO_3$ (STO) has been doped with iridium (~0.5 wt.% nominally) at the B-site and subjected to reducing conditions required for exsolution. By characterization of the system with a range of techniques including X-ray Diffraction (XRD), X-ray Photoelectron Spectroscopy (XPS), Transmission Electron Microscopy (TEM), and Scanning Transmission Electron Microscopy-Energy-Dispersive X-ray Spectroscopy (STEM-EDX), we have shown that iridium nanoparticles can be grown successfully on the surface of STO, which retains its crystal structure after exsolution. Moreover, the nanoparticles socketed to the bulk of the $SrTiO_3$ and are resistant to coalescence up to a temperature of 1300 °C in a H_2 atmosphere. Preliminary in situ TEM studies have also been carried out to gain a thorough understanding of the mechanistic steps during nanoparticle exsolution. Furthermore, as a preliminary proof of concept, the exsolved materials were tested for emission control (CO oxidation) catalysis and their activity was benchmarked against a commercially available material (1% Ir/Al_2O_3), with promising activity shown despite having only half the noble metal loading (0.5% $Ir-SrTiO_3$).

EXPERIMENTAL SECTION

Synthesis of $SrTiO_3$: The undoped $SrTiO_3$ perovskite was synthesized by solid-state reaction, mixing and grinding stoichiometric amounts of strontium carbonate ($SrCO_3$, Sigma-Aldrich, ≥99.9%) and rutile titanium (IV) oxide (TiO_2, Sigma-Aldrich, ≥99.98 %) for 30 minutes. The powders were subsequently pressed into a pellet which was calcined in air at 900 °C for 12 hours, and subsequently sintered at 1000 °C for 48 hours, with intermediate grinding and pelletizing between the two heating steps.

Synthesis and Reduction of $SrTi_{0.995}Ir_{0.005}O_3$: 0.5 % Iridium-doped strontium titanate ($Ir_{0.5}$-STO) perovskite was synthesized following a modified solid-state method. Strontium carbonate ($SrCO_3$, Sigma-Aldrich, ≥99.9 %), rutile titanium (IV) oxide (TiO_2, Sigma-Aldrich, ≥99.98 %) and iridium (IV) oxide (IrO_2, Sigma-Aldrich, ≥99.9 %) were mixed in stoichiometric amounts and fully ground for 30 minutes with agate pestle and mortar. The mixed powders were pressed into pellets (~0.7 g starting material) and subsequently calcined in air at 1000 °C for 12 h. The calcined pellets were ground for 30 minutes with agate pestle and mortar and further sintered at 1340 °C for 12 h in air, prior to pelletization. Reduction was carried out on the material in the powder form in a tube furnace using a 5% H_2/N_2 atmosphere at three temperatures, 900, 1100, and 1300 °C, for 10 h using a 5 °C/min heating and cooling rate.

Materials Characterization: Room temperature XRD patterns were acquired over a 2θ range from 20° to 80° (PANalytical X-Ray diffractometer, Cu Kα source) to confirm phase purity. The surface chemistry of the as-prepared and reduced material was analyzed by X-ray Photoelectron Spectroscopy (XPS). XPS spectra were recorded on a Thermo Scientific K-Alpha+ X-ray photoelectron spectrometer operating at 2×10^{-9} mbar base pressure. This system incorporates a monochromated, micro-focused Al Kα X-ray source (hν = 1486.6 eV) and a 180° double focusing hemispherical analyzer with a 2D detector. The X-ray source was operated at 6 mA emission current and 12 kV anode bias providing an X-ray spot size of up to 400 μm^2. Core level spectra were recorded at 20 eV pass energy. A flood gun was used to minimize the sample charging that occurs when exposing an insulated sample to an X-ray beam. The quantitative XPS analysis was performed using the Thermo Avantage software. The binding energy (B.E.) was corrected by aligning the C 1s peak of the adventitious carbon (C-C) at 284.8 eV. The intensities of the spectra were normalized to the Ti 2$p_{3/2}$ components. The microstructure of the sample was studied by high resolution SEM carried out with a JEOL JSM-6700 field emission SEM, equipped with SE and BSE detectors. The morphology and the size of the exsolved nanoparticles were determined by transmission electron microscopy (TEM) with a JEOL JEM-2100F TEM operating at a 200 kV voltage. The size distribution of the Ir nanoparticles was obtained for each of the exsolved samples ($Ir_{0.5}$-SrTiO$_3$ reduced at 900 °C, 1100 °C and 1300 °C) from TEM imaging of several perovskite grains (Ir-STO grain size ≥ 100 nm). NP diameters were extracted through ImageJ Software (https://imagej.nih.gov) and statistics were built averaging results obtained on manual selection of fully exsolved nanoparticles (n ≥ 110) imaged on grains in different areas of the TEM grid. For the purpose of the study, where faceted particles were considered the diameter was still calculated assuming a spherical shape, and for the low number of truncated octahedra structures the diameter was calculated averaging the major and minor axes accounting for an ellipsoid shape. High-resolution TEM was carried out in a FEI Titan operating at 300 kV and equipped with a Cs image aberration corrector. Elemental analysis through energy dispersive X-ray spectroscopy (EDX) in scanning-transmission electron microscopy (STEM) mode was performed to investigate the NP and the support oxide chemical composition (EDS 80 mm X-Max detector, Oxford Instruments). The samples for TEM analysis were prepared by drop-casting of powder specimens previously sonicated in high purity isopropanol onto holey carbon film copper grids (3.05 mm diam. 300 mesh, TAAB). In situ electron microscopy experiments were performed at the Center for Nanophase Materials (CNMS) in Oak Ridge National Laboratory (ORNL) using a Nion UltraSTEM 100 equipped with a C3/C5 aberration corrector operating at 100 kV voltage. The sample was prepared by dispersion of the powder in IPA, and dropcast onto a Protochips heating chip subsequently mounted on an electrical cartridge.

CO Oxidation Tests: The catalytic activity of the undoped STO, Ir-doped STO, and Ir-doped STO reduced at 900, 1100 and 1300 °C was tested using CO oxidation reaction in a fixed-bed quartz reactor (straight tube with 9 mm inner diameter) in which 10 mg of powder sample was loaded (supported by quartz wool at both sides). For comparison, a commercial Ir/Al_2O_3 catalyst (1% iridium on 5 mm alumina spheres, reduced, anhydrous, Alfa-Aesar) was also tested. All experiments were conducted at atmospheric pressure. A thermocouple (K-type) was placed in proximity to the catalyst bed to measure the sample temperature during the reaction. Another fixed-bed reactor filled with Al_2O_3 was placed upstream to this catalyst reactor, which was used to capture possible decomposed carbonyl species formed in the CO-containing gas cyl-

inders. The catalytic experiments were conducted at flow rates of 3×10^{-4} mol s^{-1} (volumetric flow rates at normal temperature and pressure (NTP) correspond to 450 cm^{3}min^{-1}). The flow rates were controlled by mass flow controllers and also measured at the outlet using a Varian digital flow meter (1000 series). To study the effect of temperature on activity, the materials were heated in an environment with an inlet gas mixture of 1% of O_2 and 0.6% of CO from 100 °C up to 450 °C. The temperature was held at each temperature step during heating, until the reaction rate became steady: i.e., the rate of CO_2 production did not vary by more than ±5% over 60 min. An XTREAM-CO_2 analyzer provided by Rosemount was used to analyze the carbon dioxide (CO_2) mole fraction in the product stream. The minimum detectable CO_2 mole fraction for the XTREAM-CO_2 analyzer was 1 ppm which corresponds to a minimum measurable rate of CO_2 production of 3×10^{-10} mol s^{-1} with typical flow rate at 3×10^{-4} mol s^{-1} (450 cm^{3}min^{-1}). The steady CO mole fraction was used to calculate conversion of CO at the temperature of measurement. Reaction rates (r_{CO_2}) in terms of CO_2 production are calculated as shown in Equation 1:

$$r_{CO_2}(\text{mol(CO}_2) \text{ s}^{-1}) = y_{CO_2} \cdot \dot{n} \qquad (1)$$

where y_{CO_2} is the measured CO_2 mole fraction at the gas outlet, $\dot{n}$ is the molar flow. Conversion was calculated as shown in Equation 2:

$$X_{CO} = 100 \cdot (y_{CO_2})/(y_{CO}) \qquad (2)$$

where y_{CO} is the CO mole fraction at the reactor inlet. The rates extracted are average rates since the composition of the reaction mixture varies along the bed. The nominal temperature of the bed and the composition of the inlet feed gas was known from direct measurements. The inlet feed gas composition did not change during the experiment. Kinetic data were extracted from the measurements collected when the reactor was operated under differential conditions (below 15%).

RESULTS AND DISCUSSION

Bulk and Surface Characterization before Exsolution

In this work, $SrTiO_3$ was doped with 0.5% of iridium, as the transition metal to be exsolved, replacing the equivalent amount of Ti^{4+} cations on the B-site ($SrIr_{0.005}Ti_{0.995}O_3$). The synthesis of 0.5% Ir-doped STO successfully resulted in the single-phase material, with characteristic diffraction signals of the $SrTiO_3$ perovskite (JCPDS 01-086-0178). After calcination at 1000 °C for 12 h, followed by sintering at 1340 °C for 12 h, the material was characterized by XRD, TEM, and XPS analysis. The X-ray diffraction pattern reported in Figure 1 (a) shows Bragg reflections consistent with the ones characteristic of reference strontium titanium oxide (JCPDS no. 01-086-0178) presented in the red pattern. The presence of only one phase indicates the successful incorporation of iridium into the perovskite lattice. A Scanning Electron Microscopy (SEM) image is reported in Figure 1 (b) to show the as-synthesized sample microstructure, whereas TEM micrographs are presented in Figure 1 (c, d). The absence of Z-contrast within the analyzed grains suggests homogeneity in sample composition, whereas the lattice fringes confirm the sample's crystallinity. STEM-EDX mapping also confirmed a homogeneous elemental distribution in the analyzed perovskite grains after synthesis (Supplementary Information Figure S2). XPS measure-

ments of Sr 3d, Ti $2p_{3/2}$ and Ir 4f core levels of the as-synthesized 0.5% Ir-doped STO are shown in Figure 1 (e-g), where they are compared to the relative core levels of the undoped $SrTiO_3$. The Sr 3d core level (Figure 1 (e)) consists of two doublets with a spin orbit splitting (SOS) of 1.75 eV. The doublet with the main component found at 132.65 eV for the undoped STO and 132.5 eV for the 0.5% Ir-doped STO can be attributed to Sr^{2+} from the lattice of $SrTiO_3$. [39, 40] The doublet with the main component found at 133.4 eV for the undoped STO and at 133.5 eV for 0.5% Ir-doped STO is most likely $SrCO_3$, consistent with what has been identified in the literature. [40] The ratio [Sr $3d_{5/2}$ SrCO$_3$: C 1s C=O] relating to the carbonate species was found to be 0.99:1.01 for the undoped STO and 0.9:1.1 for the 0.5% Ir-doped STO. Both values are close to the expected 1:1 ratio further confirming the presence of $SrCO_3$. The Ti 2p core level (Figure 1 (f)) of the undoped STO and Ir-doped STO were both fitted with one doublet with a spin orbit splitting of 5.7 eV. The position of the Ti $2p_{3/2}$ was found at B.E. of 458.15 eV and 458.05 eV for the undoped STO and Ir-doped STO, respectively. This value matches the previously reported B.E. of Ti^{4+} in $SrTiO_3$. [39, 40] The [Sr $3d_{5/2}$ (Sr lattice + SrCO$_3$) : (Ti $2p_{3/2}$ + Ir $4f_{7/2}$)] ratio was measured and found to be 0.99:1.01, which is close to the expected 1:1 ratio of $SrTi_{0.995}Ir_{0.005}O_3$. A shift to lower B.E of 0.15 eV can be noticed for both the Sr 3d and the Ti 2p between the undoped and 0.5% Ir-doped STO, which has previously been reported to be caused by oxygen vacancy formation. [41] Therefore the stoichiometry could more accurately be described by the chemical formula $SrIr_{0.005}Ti_{0.995}O_{3-\delta}$. The Ir 4f region (Figure 1 (g)) of the undoped STO shows a high contribution of the Ti $3p_{1/2}$ at B.E. of 50 eV, Ti 3s at B.E. of 61.5 eV and Ti 3s satellite at 66.7 eV. After doping the B-site of the STO with 0.5% Ir, two small components appeared at B.E. 61.8 eV and 64.7 eV, respectively, which were attributed to Ir $4f_{7/2}$ and Ir $4f_{5/2}$ in the Ir^{3+} form. [42] Interestingly, the Ir^{4+} oxidation state was not observed in the Ir 4f core level for the doped sample. The valence band was also investigated and is shown in Figure S1 (a). This shows a small peak at 1.2 eV corresponding to Ir 5d which is attributed to iridium in the +3 oxidation state ($[Xe]4f^{14}5d^6$) and/or in the +4 oxidation state ($[Xe]4f^{14}5d^5$). The fact that iridium is found in the +3 oxidation state at low doping levels is puzzling, particularly when comparing it with the Ir 4f core level of a highly-doped sample (5% Ir-doped STO). In this material (Figure S1 (b)) the presence of two doublets can be clearly observed, attributed to both Ir^{4+} and Ir^{3+} oxidation states. A more detailed investigation coupled with theoretical calculations is currently being undertaken, which will provide more insights to this phenomenon and will be the subject of discussion in future work.

Reduced $SrTi_{0.995}Ir_{0.005}O_3$ Characterization

The as-synthesized perovskite material described in the present work was investigated for B-site metal exsolution when exposed to controlled reducing conditions. Through reduction of this material under forming gas (5% H_2/N_2) at temperatures equal to and above 900 °C the emergence of metallic iridium nanoparticles could be achieved, due to depletion of the nominally B-site metal dopant from the bulk. While removing oxygen atoms from the surface (and subsequently from the bulk) through reduction, oxygen vacancies are generated allowing for the B-site cation diffusion towards the surface, where then its reduction occurs. [43] When compared to the TEM micro-
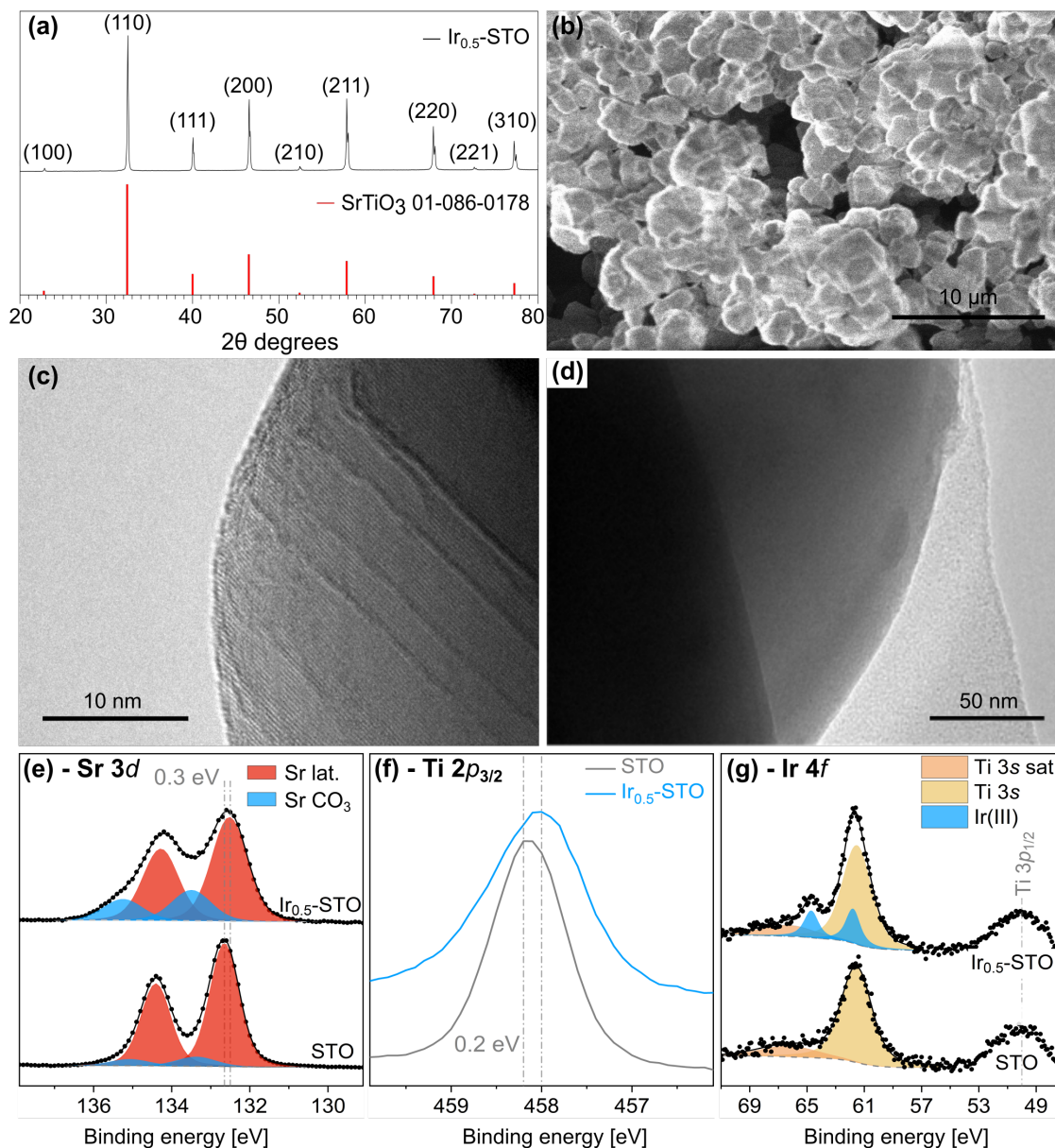
Figure 1. (a) XRD pattern acquired on the as-synthesized Ir-doped strontium titanate (black line) and reference strontium titanate pattern (red line); (b) SEM image showing the microstructure and (c), (d) TEM micrographs showing the homogeneity of the as-synthesized sample and its crystalline nature; (e), (f) and (g) XPS core levels spectra for Ir 4f, Sr 3d and Ti 2p, respectively.

graphs reported in Figure 1 (c, d) for the as-synthesized material, the reduced samples (Figure 2 (a-f)) showed presence of nanoparticles characterized by sizes ranging between 2-10 nm. The NPs were found to be uniformly distributed on the surface of the several host perovskite grains analyzed by TEM. The images show the growth of the nanoparticles occurred at the surface of the oxide structure, with a fraction of their volume often visibly submerged (or 'socketed') into the perovskite (Figure 2 (b, d, f)). These results are consistent with previous reports on similar materials, [44-46] and were explained as due to minimization of the strain energy of the support oxide. [46, 47] The effect of the three reduction temperatures is visible in the different nanoparticle size and population obtained (Figure 2 (g)), where the highest temperature (1300 °C) resulted in bigger NPs with a larger size distribution as well as higher density of nanoparticles on the perov-

skite surface compared to reduction at 1100 °C and 900 °C. Specifically, the sample reduced at 900 °C showed a size distribution of 2.36±0.84 nm, whilst a size distribution of 2.93±1.05 nm and of 4.51±2.23 nm was observed for the samples reduced at 1100 °C and 1300°C, respectively. This was expected, due to the diffusion extent being temperature dependent. [44] The increase in NP population density with T, from ~2900 μm^{-2} to ~3700 μm^{-2} and ~7400 μm^{-2} (Figure 2 (g)), suggests that at higher temperatures not only growth of NPs already on the surface is observed, but also more nuclei are formed due to further Ir diffusion, and subsequent reduction, from the bulk to the surface. This was further confirmed by the wider size distribution observed in the sample reduced at 1300 °C (Figure 2 (g)). XPS analysis was performed to further investigate the surface of the reduced materials. Figure 3 shows the (a) Sr 3d (b) Ti 2p$_{3/2}$ and (c) Ir 4f core levels
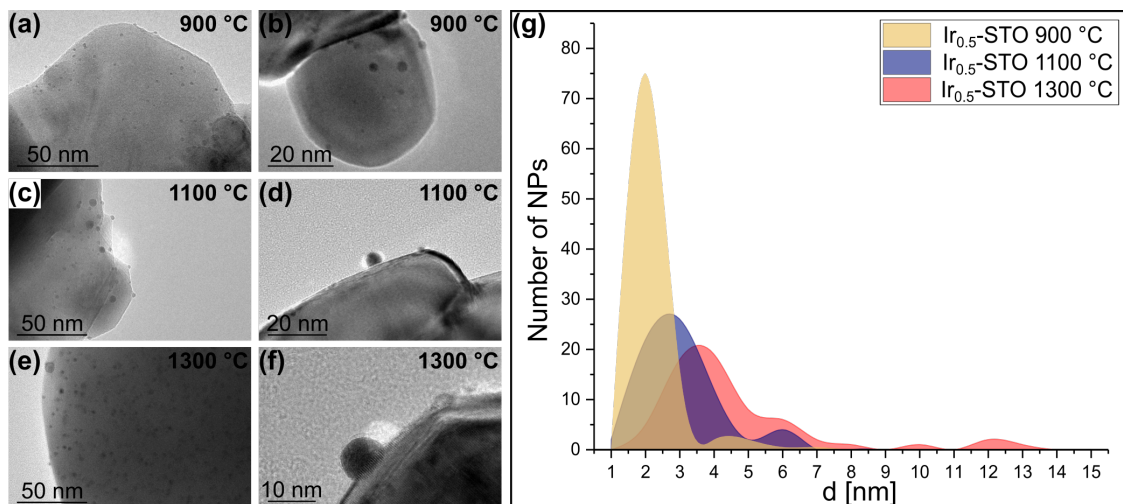
4

Figure 2. TEM micrographs of SrTi$_{0.995}$Ir$_{0.005}$O$_3$ reduced at (a-b) 900 °C, (c-d) 1100 °C and (e-f) 1300 °C under 5% H$_2$/N$_2$ atmosphere for 10 hours. (g) NP size distribution graph of the samples reduced at 900 °C, 1100 °C and 1300 °C.
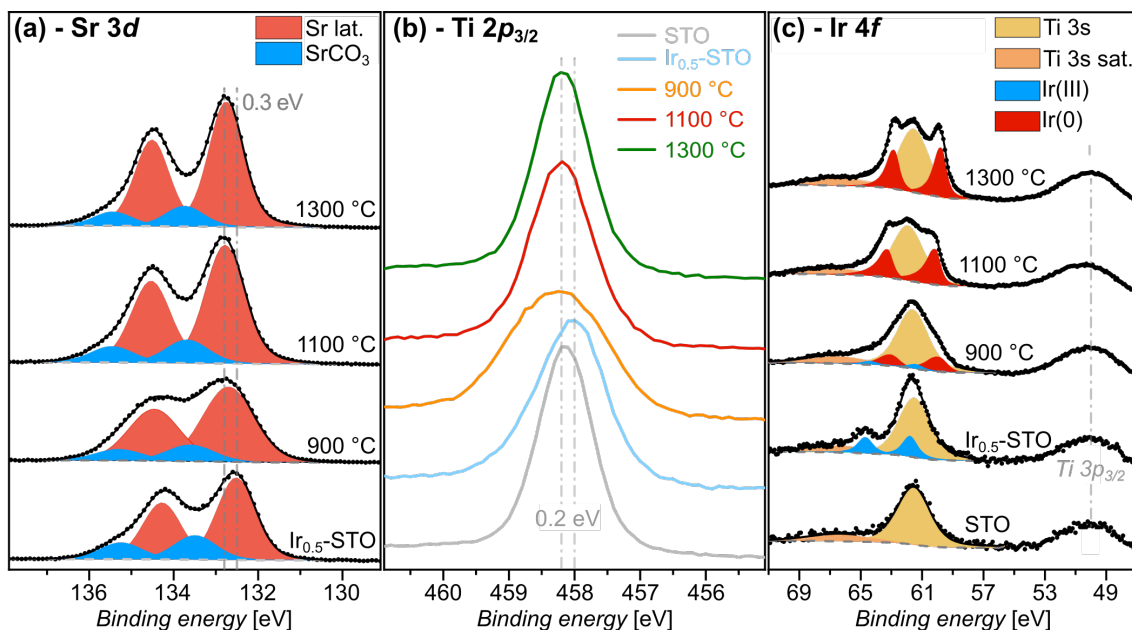

Figure 3. Evolution of the (a) Sr 3d, (b) Ti 2$p_{3/2}$, and (c) Ir 4f core levels as a function of temperature under hydrogen environment measured by XPS.

for the 0.5% Ir-doped STO before and after H$_2$ treatment. Each core level was normalized to the Ti 2$p_{3/2}$ component in order to observe any changes in the [Sr 3d: Ti 2$p_{3/2}$] and [Ir 4f: Ti 2$p_{3/2}$] ratios. After H$_2$ treatment at 900 °C, the Sr 3$d_{5/2}$, Ti 2$p_{3/2}$ and Ti 3s components showed a shift to higher B.E., closer to their corresponding values in the undoped STO, as seen in Figure 1. The [Sr 3$d_{5/2}$: Ti 2$p_{3/2}$] ratio increased from 43.0:57.0 (before reduction) to 52.2:47.8 after reduction at 1300 °C, as shown in Table 1 and Figure 4. This has been previously reported [45, 48] and can be explained by Sr^{2+} species diffusing from the bulk to fill A-site surface vacancies during reduction at high temperatures. Upon reduction at 900 °C, a broadening of the Sr 3d and Ti 2p peaks was also observed. Interestingly, this is due to sample charging, as the adventi-

tious carbon was found at 1.2 eV higher binding energy compared to its standard position (284.8 eV). Multiple measurements on the reduced materials showed that the sample H$_2$-treated at 900 °C was more prone to charging, as opposed to the ones reduced at 1100 °C and 1300 °C. Specifically, the adventitious carbon peak position was found at standard value and peak broadening was not observed for the samples reduced at higher temperatures (1100 °C and 1300°C). It is also unusual to observe charging effects in materials since the development of effective dual electron/ion charge compensation systems in XPS instruments.

In the case of Ir 4f (Figure 3 (c)), after H$_2$ treatment at 900 °C two new components appeared at 60.1 eV and 63.3 eV respectively, corresponding to metallic iridium. [49] The 3+ oxidation

5

Table 1. XPS quantification of Sr 3d5/2 : Ti 2p3/2 before Ir doping, after Ir doping and after exsolution expressed in %.

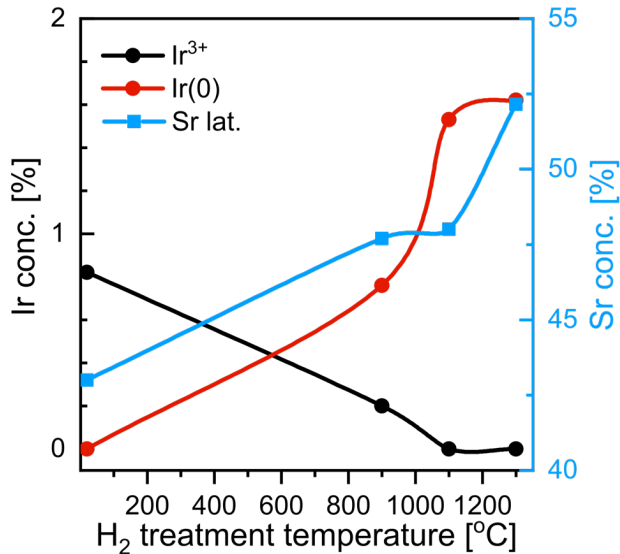| Sample	Sr Lat. : Ti	Sr SrCO₃ : Ti
Undoped STO	43.5 : 56.4	7.2 : 92.8
Ir-STO	43.0 : 57.0	19.5 : 80.5
Ir-STO, 900 °C	47.7 : 52.3	15.9 : 84.1
Ir-STO, 1100 °C	48.0 : 52.0	26.1 : 73.9
Ir-STO, 1300 °C	52.2 : 47.8	16.5 : 83.5

Figure 4. Evolution of concentration (%) of Ir^{3+} (black plot), Ir(0) (red plot), and Sr (blue plot) against Ti as a function of reduction temperature measured by XPS.

state in the Ir 4f components is still visible, although less intense, with a ratio of [Ir $4f_{7/2}$ Ir(III) : Ti $2p_{3/2}$] decreasing from 0.8:99.2 to 0.2:99.8 after H₂ treatment. As seen in Figure 4, after further reduction, the Ir^{3+} components disappear whilst, as expected, the metallic components gradually increased in intensity with increasing reduction temperature, to finally reach a ratio [Ir $4f_{7/2}$: Ti $2p_{3/2}$] of 1.6:98.4 (see Table S1). To explain the higher concentration probed by XPS on the reduced samples compared to the nominal doping concentration, calculations were performed as reported in S1 (Supporting Information). By analysis of the TEM micrographs it was possible to integrate the particles size and density (surface distribution) to estimate the number of exsolved Ir atoms per surface area, therefore allowing to correlate the XPS results reported in this section with the TEM results. Specifically, by calculating the number of exsolved Ir atoms per area of perovskite (μm⁻²), it is also possible to calculate the number of atoms analyzed in the volume of the XPS spot (400 μm² x 10 nm depth), which was found to correspond to an Ir concentration of ~2%. This agrees with the experimental result reported in Table S1 and Figure 4 (Ir concentration measured by XPS on the exsolved samples = 1.6%), therefore explaining the higher concentration on the reduced samples compared to the nominal doping. It is also interesting to notice that similar Ir metal concentrations are found for the samples reduced at 1100 °C and 1300 °C from the XPS analysis (Figure 4),

whereas NP density calculations resulted in significantly different populations (Figure 2). This can be explained by the probing depth of the XPS being 10 nm, therefore allowing for the detection of Ir metal found both on the surface and on the subsurface of the perovskite. At 1100 °C a lower number of NPs is expected (as proven by TEM analysis), although extensive Ir reduction has already occurred close to and on the surface. This results then in new NP formation at 1300 °C and/or growth of already exsolved NPs due to further Ir metal incorporation. The high-resolution TEM images (Figure 5 (a-c)) show the exsolved nanoparticles being sometimes faceted, and with a different interplanar spacing compared to the one measured for the support perovskite. Figure 5 (a, b) show the nanoparticle has grown out from the bulk lattice, with one facet partly submerged into the host, and a structure resembling a truncated octahedron (Figure 5 (b)), which has previously been reported as energetically favorable for iridium-based nanostructures. [50.] The insets in Figure 5 (c) show the separate Fast Fourier Transforms (FFT) of the support (STO) and the nanoparticle (NP), then combined in the white-outlined inset when the interface is analyzed, confirming their different structure. The interplanar spacing measured for the SrTiO₃ lattice is 0.40 nm, which agrees well with what reported for the cubic SrTiO₃ (010) lattice parameter of 0.39 nm. The nature of the nanoparticles was investigated by EDX operated in STEM mode. Figure 6 (a) reports the difference in composition between an exsolved nanoparticle and the host material. The spectra display intense iridium peaks when the analysis is performed on the nanoparticle, whereas strontium, titanium, and oxygen peaks were found as the main components of the bulk perovskite. This is also confirmed by the elemental maps obtained for the same sample region and presented in Figure 6 (b), with iridium as the only component of the nanoparticle.

In situ Electron Microscopy Study of SrTi₀.₉₉₅Ir₀.₀₀₅O₃

A preliminary in situ electron microscopy study was carried out on the as-synthesized sample, which was heated from room temperature to 1100 °C under ultra-high vacuum conditions (10⁻⁹ Torr) to reproduce a reducing environment. The data showed consistency with the results obtained ex situ, as seen in Figure 7. When heating the as-synthesized sample under ultra-high vacuum, metal clustering was initially observed occurring within the bulk, followed by their emergence on the surface at ~800 °C (Figure 7 (a)). At ~900 °C small nanoparticles were formed, with grain morphology changes observed for the support STO, as a consequence of the Ir diffusion from the bulk to the surface with subsequent restructuring of the perovskite under reducing conditions. Changes in the perovskite grain shape and size during in situ reduction have been observed for a similar structure, and have been explained as due to the perovskite tendency to sinter upon restructuring caused by exsolution. [51] At 1100 °C (Figure 7 (b)) fully exsolved nanoparticles were again found in a truncated octahedron structure, which is consistent with our ex situ results. During the in situ tests, the NP growth rate was observed to be temperature-dependent, as shown in Figure 7(c). Interestingly, when monitoring the NP size at 900 °C over a dwell time of 1.5 h, this was found to be relatively constant (inset in Figure 7 (c)), with exsolved NPs reaching a size-limit at the given temperature within the first few minutes. This is consistent with what has been observed in recent similar studies.
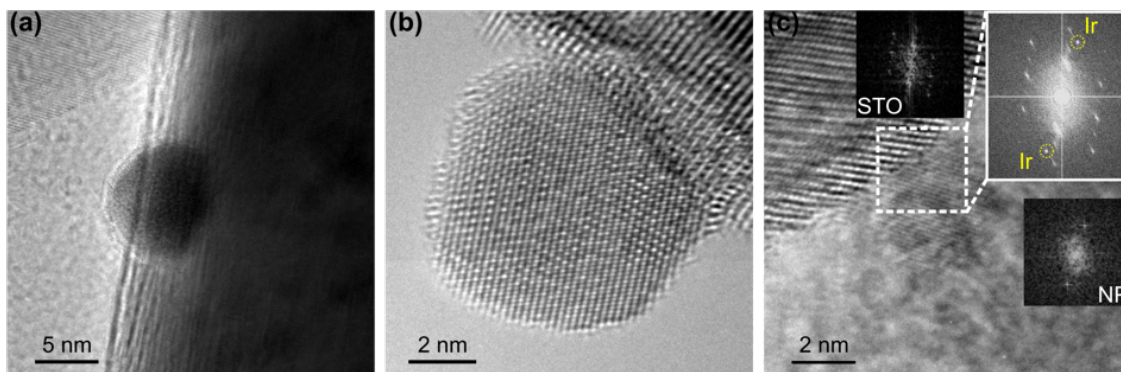
6

Figure 5. HR-TEM images showing the socketed nature of the exsolved nanoparticles (a) and the structure of the formed nanoparticles (b). The insets in (c) show the FFTs of the perovskite (STO, top left), the nanoparticle (NP, bottom right) and of the interface between the two (white boxed, top right corner).
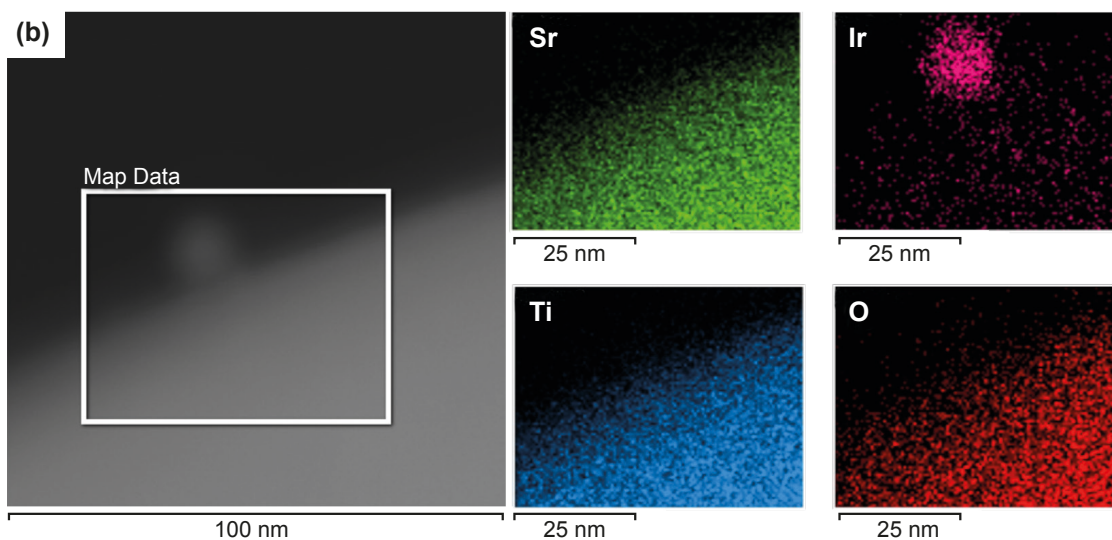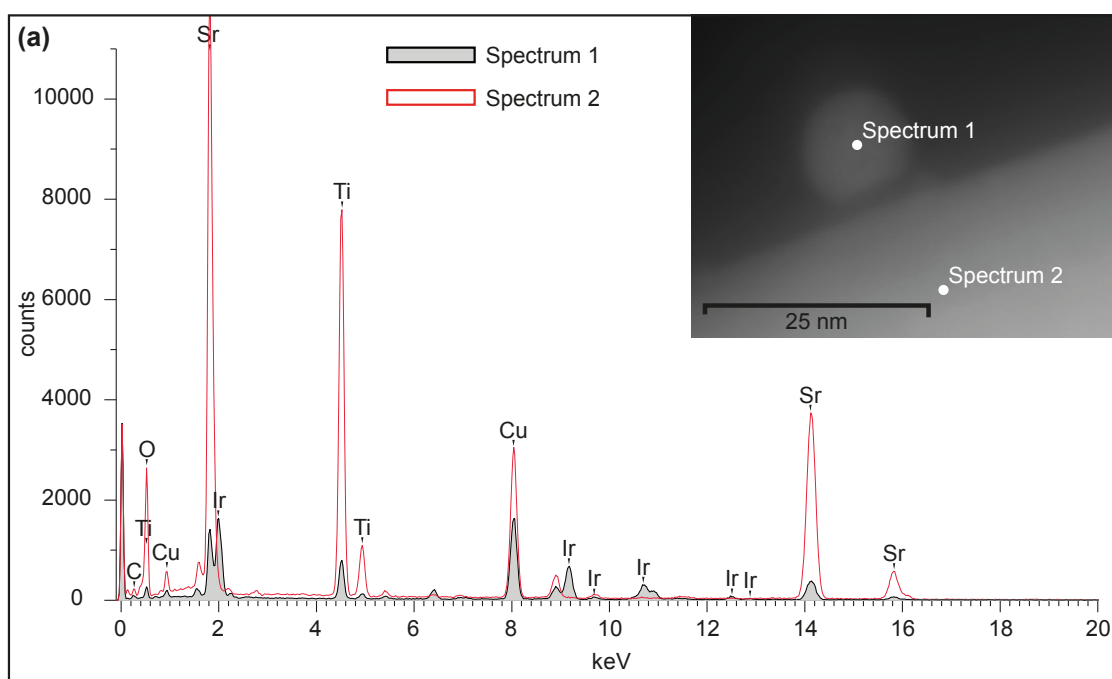

Figure 6. (a) EDX spectral analysis comparing the different composition of the emerged nanoparticle (spectrum 1) and the host perovskite (spectrum 2) from the STEM image in the inset (top right corner); (b) Elemental map analysis of the region boxed in the electron image with single element maps for Sr, Ir, Ti, and O.
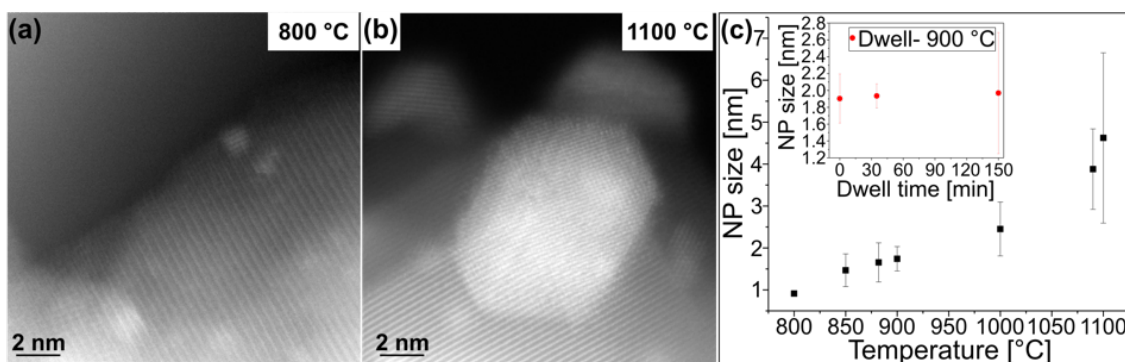
7

Figure 7. High-resolution STEM images acquired during in situ heating experiments in ultra-high vacuum. (a) Ir clusters formed on the surface of 0.5% Ir-doped STO when reached 800 °C; (b) faceted and socketed Ir NPs formed when reaching 1100 °C; (c) Size distribution graph showing the growth of the Ir NPs during the in situ electron microscopy experiment. The larger error bars at high temperatures suggest a wider size distribution developed as reduction temperature increased.
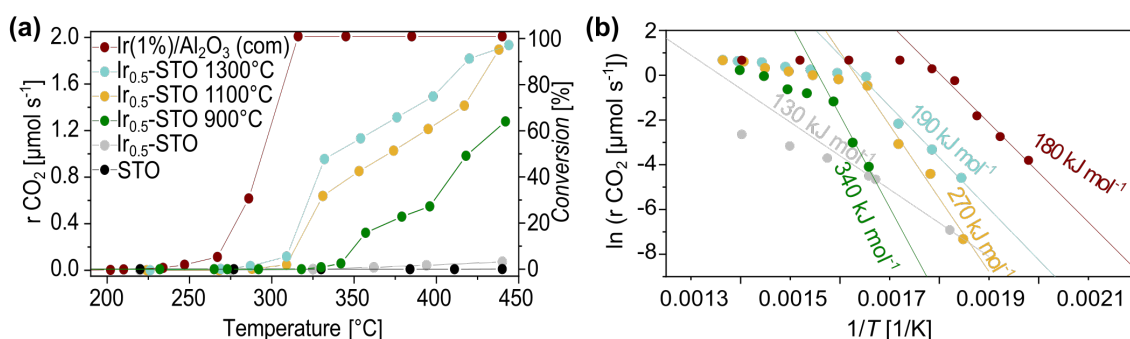

Figure 8. Catalytic activity of Ir0.5-STO applied for CO oxidation. (a) CO_2 production rates and CO conversion values as a function of temperature; note that above 10-20% conversion, rate values are not reliable due to potential mass and heat transfer limitations. (b) Arrhenius plots and activation energies calculated for data in (a) for conversions lower than 10-20%.

[43, 52] After reaching 1100 °C a wider NP size distribution was also confirmed, as shown in Figure 7 (c), again consistently with the ex situ findings shown in Figure 2. The in situ results suggest that after cluster nucleation, at lower temperatures growth occurs by diffusion and subsequent reduction of Ir atoms from the bulk to the surface to be incorporated in already formed clusters; at higher temperatures growth is, instead, observed to occur both by atom diffusion and incorporation, as well as by coalescence of NPs interacting on the perovskite surface.

Catalytic Activity Testing

The prepared materials were tested for the CO oxidation reaction, to investigate the correlation of the above-mentioned characteristics with catalytic reactivity. The samples were tested for CO oxidation under oxidizing feed conditions (0.6% CO, 1% O_2) (characteristic of catalytic converters), [53, 54] as a function of temperature. A control sample that was not doped with Ir and one that was Ir-doped but not exsolved (i.e. not reduced) as well as one commercial sample (1% Ir/Al_2O_3) were also tested under the same conditions for reference. As seen in Figure 8 the undoped sample ($SrTiO_3$) showed no measurable activity while the unexsolved sample ($Ir_{0.5}$-$SrTiO_3$) demonstrated only 2% conversion at maximum temperature, around 450 °C. On the other hand, the commercial sample was very active, reaching 100% conversion at a

temperature of 300 °C. The exsolved samples ($Ir_{0.5}$-$SrTiO_3$ 900 °C, $Ir_{0.5}$-$SrTiO_3$ 1100 °C and $Ir_{0.5}$-$SrTiO_3$ 1300 °C) show a more gradual increase in activity with temperature as compared to the commercial reference sample and also as compared to similar noble metal systems in the literature. [44, 54, 55] The $Ir_{0.5}$-$SrTiO_3$ 900 °C sample never seems to reach full conversion, whilst $Ir_{0.5}$-$SrTiO_3$ 1100 °C and $Ir_{0.5}$-$SrTiO_3$ 1300 °C samples seem to approach full conversion at a similar temperature, around 450 °C. The evidence presented in Figure 8, reporting no measurable activity observed for the un-reduced Ir-doped STO sample, clearly shows that the exsolved nanoparticles, which have emerged from the host lattice after reduction at temperatures between 900-1300 °C, are responsible for the catalytic activity observed for CO oxidation. In agreement with previously reported literature, [46, 54] these results suggest that the host perovskite mainly acts as a support, and that the catalytically active sites, on the basis of the evidence presented here, are located on the exsolved Ir metal NPs. A more detailed investigation on the active sites is of interest and will be the subject of future work. Detectable activity is first observed at 360 °C for the sample reduced at 900 °C, whilst $Ir_{0.5}$-$SrTiO_3$ 1100 °C and $Ir_{0.5}$-$SrTiO_3$ 1300 °C samples start displaying detectable activity at temperatures around 330 °C. Over the testing temperature range of 330-425 °C, the samples reduced at 1100 and 1300 °C show a similar activity evolution with temperature, with an offset of about 15% conversion in favor of the latter. This could be attributed to the higher amount of Ir

exsolved on the surface of the 1300 °C reduced sample since increasing the reduction temperature resulted in an increased total amount of metal exsolved, [46] as also confirmed by XPS and TEM results. This is consistent with results reported for similar exsolved perovskites, [46] where higher exposed metal coverage resulted in higher catalytic activity. Similar reports in the literature also suggest that the high activity observed from exsolved NPs on perovskite oxides is also related to the strain imposed by the socketing feature of these structures. [4, 46, 56] Arrhenius plots of the sample activities from data corresponding to lower than 10-20% conversion is shown in Figure 8 (b). The activation energy corresponds to Ea ranging from ~130 kJ mol^{-1} for the unexsolved sample to ~340 kJ mol^{-1} for the sample reduced at 900 °C, ~270 kJ mol^{-1} for the one reduced at 1100 °C, and ~190 kJ mol^{-1} for the 1300 °C reduced sample. Literature reports demonstrate activation energies for the CO oxidation reaction of the order of 100 kJ mol^{-1}, [57] while Ea values close to 150 kJ mol^{-1} are characteristic of CO desorption energy from oxide surfaces. [58] The relatively high Ea values observed here could also be characteristic of supports with low reducibility, as has been observed before for exsolved systems. [44] When compared to the commercial sample, this has a lower temperature activation energy of Ea=130 kJ mol^{-1}. Comparison with the exsolved samples verifies the fact that our materials do not exhibit characteristic noble metal behaviour [54] and could indicate that the support and probably the interaction between the support and the exsolved particles governs the profile of those curves and, as a consequence, their activity. This has been demonstrated before in exsolved materials for analogous applications. [44] Moreover, the fact that the exsolved materials reported a lower activity compared to the commercial catalyst can be explained by considering that only a fraction of the nominal Ir doping amount is exsolved, and therefore exposed on the surface, during reduction. Specifically, only ~0.2% of the nominal 0.5% Ir doping has been calculated to exsolve at the highest temperature investigated in this work, based on estimate of exsolved Ir metal per Ir-STO surface area (calculations in S1). This is five times less compared to the 1% Ir deposited on the surface of the commercial catalyst, and so the high activity displayed by our catalyst might be explained by the strained nature of the exsolved NPs when compared to top-down deposited NPs, also previously observed in similar materials. [44, 59] Additionally, this was verified by the fact that the activity of the samples increased with the increase in the reduction temperature, due to an increase in the amount of metal exsolved per surface area. Overall, this work provides a novel structure where the design of Ir-based perovskites with an extremely low noble metal amount (~0.5% weight) is made possible by Ir incorporation in the lattice, subsequently exsolved as high-specific-surface-area metallic nanoparticles. These were then demonstrated to have catalytic activity for the CO oxidation reaction. The preliminary results reported in this section are a promising starting point for the optimization of Ir-doped perovskites with such dilute active noble metal doping and their possible future applications in catalysis.

CONCLUSIONS

In this work we have demonstrated the successful exsolution of Ir nanoparticles from SrTiO₃. The synthesis of this material resulted in a single-phase homogeneous perovskite, con-

firming successful incorporation of the dopant in the ABO₃ structure. Following reduction, the formation of socketed and faceted metallic iridium nanoparticles was obtained, and this was studied both ex situ and in situ, with emergence of densely distributed surface nanoparticles from 900 °C upwards. The reduced material was extensively characterized by TEM, STEM-EDX, and XPS, and insights of the NP emergence mechanism were obtained by preliminary in situ heating STEM experiments. The exsolved material presented in this work exhibited promising catalytic activity (conversion for CO oxidation), despite having five time less nominal surface loading than a 1% Ir/Al₂O₃ commercial catalyst, as only 0.2% of iridium is actually exposed on the surface of the exsolved Ir$_{0.5}$-STO. Overall, the distinctive socketing between the metal catalyst and the STO support, and the performance of the 0.5% Ir-doped STO reported here show the promise for this material to be tested for other catalytic applications, such as water splitting, electrocatalysis for OER, and reforming reactions for syngas and/or hydrogen production.

ASSOCIATED CONTENT

Supporting Information

The Supporting Information is available free of charge on the ACS Publications website.

Image analysis and calculations; XPS supplementary data; STEM-EDX maps of as-synthesised Ir$_{0.5}$-STO (PDF)

AUTHOR INFORMATION

Corresponding Authors

* E-mail: e.cali14@imperial.ac.uk (E.C.)
* E-mail: d.payne@imperial.ac.uk (D.J.P.)

Notes
There are no conflicts of interest to declare.

REFERENCES

[1]   G. Tsekouras, D. Neagu, J. T. S. Irvine. Step-Change in High Temperature Steam Electrolysis Performance of Perovskite Oxide Cathodes with Exsolution of B-site Dopants. *Energy Environ. Sci.* **2012**, 6, 256-266.

[2]   D. Neagu, G. Tsekouras, D. N. Miller, H. Ménard, J. T. S. Irvine. In Situ Growth of Nanoparticles through Control of Non-Stoichiometry. *Nat. Chem.* **2013**, 5, 916-923.

[3]   B. Madsen, W. Kobsiriphat, Y. Wang, L. Marks, S. Barnett. Nucleation of Nanometer-Scale Electrocatalyst Particles in Solid Oxide Fuel Cell Anodes. *J. Power Sources* **2007**, 166, 64-67.

[4]   D. Neagu, T.-S. Oh, D. N. Miller, H. Ménard, S. M. Bukhari, S. R. Gamble, R. J. Gorte, J. M. Vohs, J. T.S. Irvine. Nano-Socketed Nickel Particles with Enhanced Coking Resistance Grown In Situ by Redox Exsolution. *Nature Commun.*, **2015**, 6, 1-8.

[5]   L. Ye, M. Zhang, P. Huang, G. Guo, M. Hong, C. Li, J. T. S. Irvine, K. Xie. Enhancing CO_2 Electrolysis through Synergistic Control of Non-Stoichiometry and Doping to Tune Cathode Surface Structures. *Nature Commun.*, **2017**, 8, 14785, 1-10.

[6]   J. T. S. Irvine, D. Neagu, M. C. Verbraeken, C. Chatzichristodoulou, C. Graves, M. B. Mogensen. Evolution of the Electrochemical Interface in High-Temperature Fuel Cells and Electrolysers. *Nat Energy*, **2016**, 1(1), 1-13.

[7]   J. Myung, D. Neagu, D. N. Miller, J. T. S. Irvine. Switching on Electrocatalytic Activity in Solid Oxide Cells. *Nature*, **2016**, 537, 528-531.

[8]   O. Kwon, S. Sengodan, K. Kim, G. Kim, H. Y. Jeong, J. Shin, Y. Ju, J. W. Han, G. Kim. Exsolution Trends and Co-Segregation Aspects of Self-Grown Catalyst Nanoparticles in Perovskites. *Nat. Commun.*, **2017**, 8(1), 1-7.

[9]   H. Tanaka, M. Uenishi, M. Taniguchi, I. Tan, K. Narita, M. Kimura, K. Kaneko, Y. Nishihata, J. Mizuki. The Intelligent Catalyst Having the Self-Regenerative Function of Pd, Rh and Pt for Automotive Emissions Control. *Catal. Today*, **2006**, 117, 321-328.

[10]   R. Glaser, T. Zhu, H. Troiani, A. Caneiro, L. Mognib S. Barnett. The Enhanced Electrochemical Response of Sr(Ti$_{0.3}$Fe$_{0.7}$Ru$_{0.07}$)O$_{3−δ}$ Anodes due to Exsolved Ru–Fe Nanoparticles. *J. Mater. Chem. A*, **2018**, 6, 5193-5201.

[11]   F. Kosaka, N. Noda, T. Nakamura, J. Otomo. In Situ Formation of Ru Nanoparticles on La$_{1−x}$Sr$_x$TiO$_3$-Based Mixed Conducting Electrodes and their Application in Electrochemical Synthesis of Ammonia Using a Proton-conducting Solid Electrolyte. *J. Mater. Sci.*, **2017**, 52, 2825-2835.

[12]   G. Yang, J. Wang, Y. Lyu, K. Lama, F. Ciucci. In Situ Growth of Pt$_3$Ni Nanoparticles on an A-Site Deficient Perovskite with Enhanced Activity for the Oxygen Reduction eaction. *J. Mater. Chem. A*, **2017**, 5, 6399-6404.

[13]   I. Ali, K. AlGhamdi, F. T. Al-Wadaania. Advances in Iridium Nano Catalyst Preparation, Characterization and Applications. *J. Mol. Liq.*, **2019**, 280, 274-284.

[14]   P. Lettenmeier, J. Majchel, L. Wang, V. A. Saveleva, S. Zafeiratos, E. R. Savinova, J.-J. Gallet, F. Bournel, A. S. Gago, K. A. Friedricha. Highly Active Nano-Sized Iridium Catalysts: Synthesis and Operando Spectroscopy in a Proton Exchange Membrane Electrolyzer. *Chem. Sci.*, **2018**, 9, 3570-3579.

[15]   T. Yang, Y. Ma, Q. Huang, G. Cao. Palladium–Iridium Nanocrystals for Enhancement of Electrocatalytic Activity toward Oxygen Reduction Reaction. *Nano Energy*, **2016**, 19, 257-268.

[16]   R. Badam, M. Hara, H. H. Huang, M. Yoshimura. Synthesis and Electrochemical Analysis of Novel IrO$_2$ Nanoparticle Catalysts Supported on Carbon Nanotube for Oxygen Evolution Reaction. *Int. J. Hydrog. Energy*, **2018**, 43, 18095-18104.

[17]   S. Cherevko, S. Geiger, O. Kasian, N. Kulyk, J. P. Grote, A. Savan, B.R. Shrestha, S. Merzlikin, B. Breitbach, A. Ludwig, K. J. J. Mayrhofer. Oxygen and Hydrogen Evolution Reactions on Ru, RuO$_2$, Ir, and IrO$_2$ Thin Film Electrodes in Acidic and Alkaline Electrolytes: A Comparative Study on Activity and Stability. *Catal. Today*, 2016, 262, 170-180.

[18]   F.-D. Kong, S. Zhang, G.-P. Yin, N. Zhang, Z.-B. Wang, C.-Y. Du. Pt/Porous-IrO$_2$ Nanocomposite as Promising Electrocatalyst for Unitized Regenerative Fuel Cell. *Electrochem. Commun.*, **2012**, 14, 63-66.

[19]   D. Dang, L. Zhang, X. Zeng, X. Tian, C. Qu, H. Nan, T. Shu, S. Hou, L. Yang, J. Zeng, S. Liao. In Situ Construction of Ir@ Pt/C Nanoparticles in the Cathode Layer of Membrane Electrode Assemblies with Ultra-Low Pt Loading and High Pt Exposure. *J. Power Sources*, **2017**, 355, 83-89.

[20]   A. Kiderys, M. Kot, E. Janiszewska, M. Pietrowski, C. Yang, M. Zieliński. SBA Materials as Support of Iridium Catalyst for Hydrogenation Reactions. *Catal. Today*, **2019**, DOI: 10.1016/j.cattod.2019.03.018

[21]   K. Nakagawa, K. Anzai, N. Matsui, N. Ikenaga, T. Suzuki, Y. Teng, T. Kobayashi, M. Haruta. Effect of Support on the Conversion of Methane to Synthesis Gas over Supported Iridium Catalysts. *Catal. Lett.*, **1998**, 51, 163-167.

[22]   G. Postole, T. S. Nguyen, M. Aouine, P. Gélin, L. Cardenas, L. Piccolo. Efficient Hydrogen Production from Methane over Iridium-Doped Ceria Catalysts Synthesized by Solution Combustion. *Appl. Catal. B Environ.*, **2015**, 166-167, 580-591.

[23]   G. Goula, P. Katzourakis, N. Vakakis, T. Papadam, M. Konsolakis, M. Tikhov, I. V. Yentekakis. The Effect of Potassium on the Ir/C$_3$H$_6$+ NO+ O$_2$ Catalytic System. *Catal. Today*, **2007**, 127, 199-206.

[24]   I. Tomska-Foralewska, M. Zieliński, M. Pietrowski, W. Przystajko, M. Wojciechowska. Iridium Supported on MgF$_2$–MgO as Catalyst for CO Oxidation. *Catal. Today*, **2011**, 176, 263-266.

[25]   C. Wögerbauer, M. Maciejewski, M. M. Schubert, A. Baiker. Effect of Sodium on the Catalytic Properties of Iridium Black in the Selective Reduction of NOx by Propene under Lean-burn Conditions. *Catal. Lett.*, **2001**, 74, 1-7.

[26]   C. Wögerbauer, M. Maciejewski, A. Baiker, U. Göbel. Ir/H-ZSM-5 Catalysts in the Selective Reduction of NOx with Hydrocarbons. *Top. Catal.*, **2001**, 16, 181-186.

[27]   T. Ioannides, A. Efstathiou, Z. Zhang, X Verykios. CO Oxidation over Rh Dispersed on SiO$_2$, Al$_2$O$_3$ and TiO$_2$: Kinetic Study and Oscillatory Behavior. *J. Catal.*, **1995**, 156, 265-272.

[28]   B. Chen, L. A. Crosby, C. George, R. M. Kennedy, N. M. Schweitzer, J. Wen, R. P. Van Duyne, C. Stair, K. R. Poeppelmeier, L. D. Marks, M. J. Bedzyk. Morphology and CO Oxidation Activity of Pd Nanoparticles on SrTiO$_3$ Nanopolyhedra. *ACS Catal.*, **2018**, 8, 6, 4751-4760.

[29]   J. Yang, V. Tschamber, D. Habermacher, F. Garin, P. Gilot. Effect of Sintering on the Catalytic Activity of a Pt Based Catalyst for CO Oxidation: Experiments and Modeling. *Appl. Catal. B Environ.*, **2008**, 83, 229-239.

[30]   I. V. Yentekakis, G. Goula, S. Kampouri, I. Betsiargyropoulou, P. Panagiotopoulou, M. J. Taylor, G. Kyriakou, R. M. Lambert. Ir-Catalysed Nitrous Oxide (N$_2$O) Decomposition: Effect of Ir Particle Size and Metal–Support Interactions. *Catal. Lett.*, **2018**, 148, 341-347.

[31]   M. Okumura, N. Masuyama, E. Konishi, S. Ichikawa, T. Akita. CO oxidation below room temperature over Ir/TiO$_2$ catalyst prepared by deposition precipitation method. J. Catal., **2002**, 208, 485-489.

[32]   Y. Lu, J. Wang, L. Yu, L. Kovarik, X. Zhang, A. S. Hoffman, A. Gallo, S. R. Bare, D. Sokaras, T. Kroll, V. Dagle, H. Xin, A. M. Karim. Identification of the Active Complex for CO Oxidation over Single-Atom Ir-on-MgAl$_2$O$_4$ Catalysts. *Nat. Catal.*, **2019**, 2, 149-156.

[33]   W. Zhang, A. Wang, L. Li, X. Wang, T. Zhang. Promoting Role of Fe in the Preferential Oxidation of CO Over Ir/Al$_2$O$_3$. *Catal. Lett.*, **2008**, 121, 319-323.

[34]   Y. Huang, A. Wang, L. Li, X. Wang, D. Su, T. Zhang. Ir-in-Ceria: A Highly Selective Catalyst for Preferential CO Oxidation. *J. Catal.*, **2008**, 255, 144-152.

[35]   S. B. Singh, *gctl*, **2016**, 2, 206.

[36]   S. Geiger, O. Kasian, M. Ledendecker, E. Pizzutilo, A. M. Mingers, W. T. Fu, O. Diaz-Morales, Z. Li, T. Oellers, L. Fruchter, A. Ludwig, K. J. J. Mayrhofer, M. T. M. Koper, S. Cherevko. The Stability Number as a Metric for Electrocatalyst Stability Benchmarking. *Nat. Catal.*, **2018**, 1, 508-515.

[37]   L. C. Seitz, C. F. Dickens, K. Nishio, Y. Hikita, J. Montoya, A. Doyle, C. Kirk, A. Vojvodic, H. Y. Hwang, J. K. Norskov, T. F. Jaramillo. A Highly Active and Stable IrOx/SrIrO$_3$ Catalyst for the Oxygen Evolution Reaction. *Science*, **2016**, 353, 1011-1014.

[38]   S. M. Alia, B. Rasimick, C. Ngo, K. C. Neyerlin, S. S. Kocha, S. Pylypenko, H. Xu, B. S. Pivovara. Activity and Durability of Iridium Nanoparticles in the Oxygen Evolution Reaction. *J. Electrochem. Soc.*, **2016**, 163, F3105.

[39]   R. Vasquez. SrTiO$_3$ by XPS. *Surf. Sci. Spectra*, **1992**, 1, 129-135.

[40] P. V. Nagarkar, P. C. Searson, F. D. Gealy. Effect of Surface Treatment on SrTiO$_3$: An X-Ray Photoelectron Spectroscopic Study. *J. Appl. Phys.*, **1991**, 69, 459-462.

[41] H. Tan, Z. Zhao, W. Zhu, E. N. Coker, B. Li, M. Zheng, W. Yu, H. Fan, Z. Sun. Oxygen Vacancy Enhanced Photocatalytic Activity of Pervoskite SrTiO$_3$. *ACS Appl. Mater. Interfaces*, **2014**, 6, 19184-19190.

[42] S. Kawasaki, R. Takahashi, K. Akagi, J. Yoshinobu, F. Komori, K. Horiba, H. Kumigashira, K. Iwashina, A. Kudo, M. Lippmaa. Electronic Structure and Photoelectrochemical Properties of an Ir-doped SrTiO$_3$ Photocatalyst. *J. Phys. Chem. C*, **2014**, 118, 20222-20228.

[43] D. Neagu, V. Kyriakou, I. L. Roiban, M. Aouine, C. Tang, A. Caravaca, K. Kousi, I. Schreur-Piet, I. S. Metcalfe, P. Vernoux, M. C. M. van de Sanden, M. N. Tsampas. In situ observation of nanoparticle exsolution from Perovskite oxides: from atomic scale mechanistic insight to nanostructure tailoring. *ACS Nano*, **2019**, 13, 12996-13005.

[44] C. Tang, K. Kousi, D. Neagu, J. Portolés, E. I. Papaioannou, I. S. Metcalfe. Towards Efficient Use of Noble Metals via Exsolution Exemplified for CO Oxidation. *Nanoscale*, **2019**,11, 16935-16944.

[45] D. Neagu, T. Oh, D. N. Miller, H. Ménard, S- M. Bukhari, S. R. Gamble, R. J. Gorte, J. M. Vohs, J. T.S. Irvine. Nano-Socketed Nickel Particles with Enhanced Coking Resistance Grown In Situ by Redox Exsolution. *Nat. Commun.*, **2015**, 6(1), 1-8.

[46] T. Oh, E. K. Rahani, D. Neagu, J. T. S. Irvine, V. B. Shenoy, R. J. Gorte, J. M. Vohs. Evidence and Model for Strain-Driven Release of Metal Nanocatalysts from Perovskites during Exsolution. *J. Phys. Chem. Lett.*, **2015**, 6, 5106-5110.

[47] T. M. Onn, M. Monai, S. Dai, E. Fonda, T. Montini, X. Pan, G. W. Graham, P. Fornasiero, R. J. Gorte. Smart Pd Catalyst with Improved Thermal Stability Supported on High-Surface-Area LaFeO$_3$ Prepared by Atomic Layer Deposition. *J. Am. Chem. Soc.*, **2018**, 140, 4841-4848.

[48] Y. Gao, Z. Lu, T. L. You, J. Wang, L. Xie, J. He, F. Ciucci. Energetics of Nanoparticle Exsolution from Perovskite Oxides. *J. Phys. Chem. Lett.*, **2018**, 9, 3772-3778.

[49] S. J. Freakley, J. Ruiz-Esquius, D. J. Morgan. The X-ray Photoelectron Spectra of Ir, IrO$_2$ and IrCl$_3$ revisited. *Surf. Interface Anal.*, **2017**, 49, 794-799.

[50] T. Yang, G. Cao, Q. Huang, Y. Ma, S. Wan, H. Zhao, N. Li, F. Yin, X. Sun, D. Zhang, M. Wang. Truncated Octahedral Platinum–Nickel–Iridium Ternary Electro-Catalyst for Oxygen Reduction Reaction. *J. Power Sources*, **2015**, 29, 201-208.

[51] S. Dai, S. Zhang, M. B. Katz, G. W. Graham, X. Pan. In Situ Observation of Rh-CaTiO$_3$ Catalysts during Reduction and Oxidation Treatments by Transmission Electron Microscopy. *ACS Catal.*, **2017**, 7, 1579-1582.

[52] Y. R. Jo, B. Koo, M. J. Seo, J.K. Kim, S. Lee, K. Kim, J.W. Han, W. Jung, B. J. Kim. Growth Kinetics of Individual Co Particles Ex-Solved on SrTi$_{0.75}$Co$_{0.25}$O$_{3-\delta}$ Polycrystalline Perovskite Thin Films. *JACS*, **2019**, 141, 6690-6697.

[53] J. B. Heywood. Pollutant Formation and Control in Spark-Ignition Engines. *Energy and Combustion Science*, Elsevier, **1979**.

[54] D. Neagu, E. I. Papaioannou, W. K. W. Ramli, D. N. Miller, B. J. Murdoch, H. Ménard, A. Umar, A. J. Barlow, P. J. Cumpson, J. T. S. Irvine, I. S. Metcalfe. Demonstration of Chemistry at a Point through Restructuring and Catalytic Activation at Anchored Nanoparticles. *Nat. Commun.*, **2017**, 8(1), 1-8.

[55] S. Royer, D. Duprez. Catalytic Oxidation of Carbon Monoxide over Transition Metal Oxides. ChemCatChem, **2011**, 3, 24-65.

[56] E. I. Papaioannou, D. Neagu, W. K. W. Ramli, J. T. S. Irvine and I. S. Metcalfe. Sulfur-Tolerant, Exsolved Fe–Ni Alloy Nanoparticles for CO Oxidation. *Top. Catal.*, **2019**, 62, 1149-1156.

[57] N. W. Cant, P. Hicks, B. Lennon. Steady-State Oxidation of Carbon Monoxide over Supported Noble Metals with Particular Reference to Platinum. *J. Catal.*, **1978**, 54, 372-383.

[58] P. J. Berlowitz, C. H. Peden, D. W. Goodman. Kinetics of Carbon Monoxide Oxidation on Single-Crystal Palladium, Platinum, and Iridium. *J. Phys. Chem.*, **1988**, 92, 5213-5221.

[59] B.H. Yan, Q.Y. Wu, J.J. Cen, J. Timoshenko, A.I. Frenkel, D. Su, X.Y. Chen, J.B. Parise, E. Stach, A. Orlov, J.G. Chen. Highly Active Subnanometer Rh Clusters Derived from Rh-Doped SrTiO$_3$ for CO$_2$ Reduction. *Appl. Catal. B*, **2018**, 237, 1003-1011.